Chemical Engineering Journal 394 (2020) 124877

Contents lists available at ScienceDirect

Chemical Engineering Journal

journal homepage: www.elsevier.com/locate/cej

Efficient and regenerative near-infrared glass-ceramic photocatalyst fabricated by a facile in-situ etching method

Guobiao Li[a], Shouqiang Huang[b], Haiping Yuan[a], Nanwen Zhu[a,c,*], Yancen Wei[a]

[a] Shanghai Engineering Research Center of Solid Waste Treatment and Resource Recovery, School of Environmental Science and Engineering, Shanghai Jiao Tong University, Shanghai 200240, PR China
[b] School of Chemistry and Environmental Engineering, Jiangsu University of Technology, Changzhou, Jiangsu 213001, PR China
[c] Shanghai Institute of Pollution Control and Ecological Security, Shanghai 200092, PR China

HIGHLIGHTS

- An innovative self-crystallized upconversion luminescence SBBO GC is studied.
- GC15 obtains from facile in-situ etching method that possess core-shell structure.
- The MO degradation rate of GC15 is 79% under NIR irradiation for 90 min.
- GC15 can be easily regenerated and high photocatalytic activity will be maintained.
- The NIR GC photocatalyst is suitable for large-scale production.

GRAPHICAL ABSTRACT

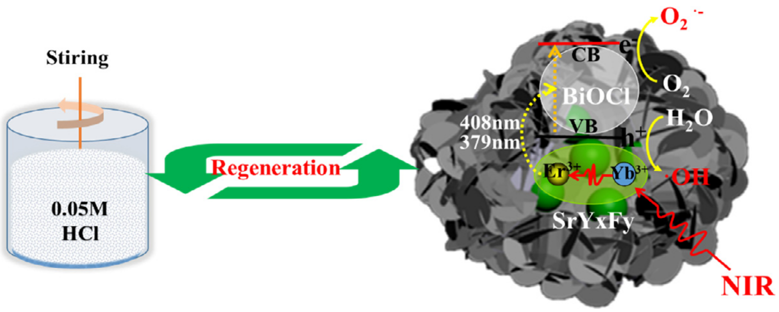

ARTICLE INFO

Keywords:
NIR GC photocatalyst
Regenerative
Large-scale fabrication
Glass-ceramic

ABSTRACT

Low cost and large-scale fabrication of high-efficiency near-infrared (NIR) photocatalysts are especially promising for the degradation of organic pollutants. Herein, a facile in-situ etching method by growing BiOCl nanosheets on self-crystallized upconversion SrO-Bi_2O_3-B_2O_3 (SBBO) glass-ceramic (GC) is developed to synthesize an efficient NIR GC photocatalyst. Through structure and morphology characterizations, it is found that the NIR GC photocatalyst possesses the core-shell structure, where the SBBO GC micro-powder including optically active centers (Er^{3+}, Yb^{3+}, and Y^{3+}) doped SrF_2 nanocrystals are displayed as the core, and the BiOCl is as the superficial coating. The NIR GC photocatalysts can efficiently harvest the NIR photons and emit strong UV (379 nm), violet (408 nm), green (523 and 540 nm), and red (656 nm) light, which are able to be utilized by themselves for photocatalysis. In the degradation of organic pollutants under NIR irradiation for 90 min, high removal rates of 66% (antibiotic norfloxacin) and 79% (methyl orange) are achieved. Furthermore, the NIR GC photocatalyst can be facile regenerated by using HCl etching again, and suitable for large-scale fabrication that will supply a new strategy for development of efficient photocatalyst.

1. Introduction

Heterogeneous photocatalysis has provided a promising approach to solve the problems in the fields of environment remediation and energy production [1], in which many efforts have been put into remodeling crystal lattice, surface, and interface of photocatalysts to broaden their

---

[*] Corresponding author at: Shanghai Engineering Research Center of Solid Waste Treatment and Resource Recovery, School of Environmental Science and Engineering, Shanghai Jiao Tong University, Shanghai 200240, PR China.

E-mail address: nwzhu@sjtu.edu.cn (N. Zhu).

https://doi.org/10.1016/j.cej.2020.124877
Received 18 November 2019; Received in revised form 17 March 2020; Accepted 22 March 2020

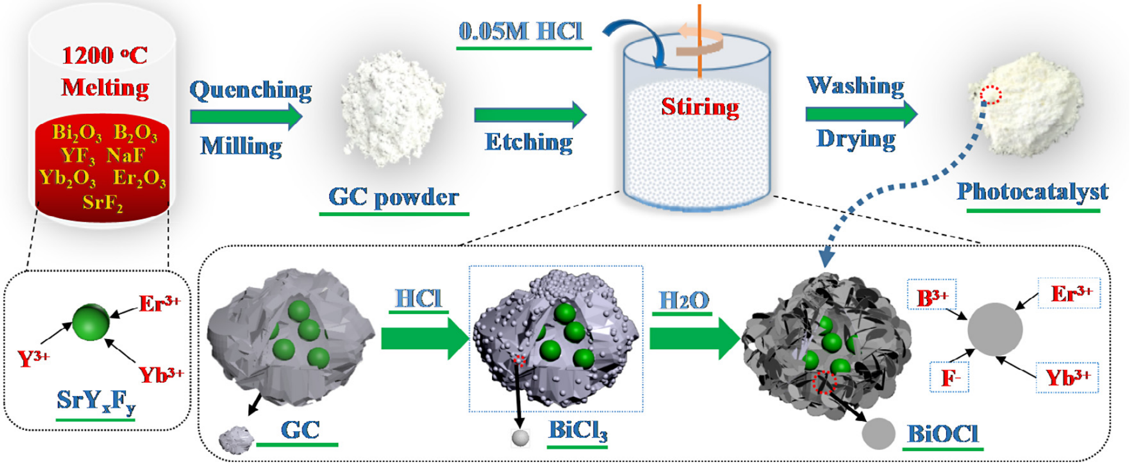

Fig. 1. Schematic illustration for the preparation of GC and photocatalyst, in which the photographs of GC powder and photocatalyst were present.

light absorption wavelengths, design active reaction sites, and control the electron-hole (e-h^+) pair separation [2]. Most of these semiconductor photocatalysts require ultraviolet (UV)- or visible-light activation, however, the use of the light irradiation has intrinsic challenges, such as the low penetration of UV and visible light, which greatly inhibit the wide application of photocatalysis [3]. It should be noted that this problem may be overcome by the utilization of near-infrared (NIR) light, which has a much higher penetration depth through various media, notably biological tissue and wastewater [4]. Construction of NIR light responsive upconversion photocatalyst has been proved to be an effective way to improve photocatalytic efficiency, owing to their successive absorption of low-energy NIR photons to the subsequent emission of UV and visible photons with higher energies, and the NIR-driven degradation of organic pollutants can be realized to enhance the entire photocatalytic efficiency under UV-vis-NIR light irradiation [3,5–8]. Meanwhile, NIR photocatalysts have the capacity to capture the deeply penetrated NIR light and utilize the upconverted high-energy photons to maintain photoactivity, even when the surface of photocatalyst is obstructed by pollutant [9]. However, the traditional NIR photocatalysts have drawbacks of the tedious preparation process and low photocatalytic efficiency under NIR irradiation. An innovative fabrication approach with convenient and low cost should be explored for the high-efficiency NIR photocatalyst.

It has been reported that BiOCl can be grown on the Bi or Bi_2O_3 films via reacting with the Cl^- ions contained solutions [10–12], where the growing mechanism was suggested to be a nucleation-dissolution-recrystallization process. However, these processes involve multiple steps and complex operations, which may not be suitable for practical large-scale fabrication. Glass-ceramic (GC) is a special glass material that has both glass and crystal structures formed in the glass crystallization process. Notably, the practical production technology of GC has been very mature and can be easily carried out for large-scale preparation of GC products, such as the widely used floor and electric furnace heat conductive plates in our daily life. It has been reported that BiOCl could be grown on the surface of the SrO-Bi_2O_3-B_2O_3 (SBBO) self-cleaning glass pane by HCl etching [13]. It is noted that although the fabrication cost of SBBO GC is lower than those of the Bi_2O_3 and Bi films, all their photocatalytic performances are still poor because of their low light utilization efficiency and small specific surface area. The SBBO GC belongs to the polar space group P63 [14], and has the potential applications of transparent glass and glass-nano/microcrystal composites in view [15]. The conductivity analysis had proposed that the charge transport occurred in SBBO GC through the participation of non-bridging oxygen NBO, and the stretched exponential behavior appeared to be a direct consequence of the NBO switching mechanism of charge transport [15]. The SBBO GC with appropriate properties of charge transport and dielectric relaxation, may contribute to the separation of electron-hole (e^--h^+) pair of BiOCl when BiOCl growing on its surface.

Interestingly, the lanthanides-doped GC sample containing luminescent nanocrystals (i.e., fluorides of $NaYF_4$, CaF_2, SrF_2 or $SrYF_5$) is attractive for upconversion matrices, because these luminescent nanocrystals were directly crystallized in GC and they have stable structure to maintain high upconversion luminescence [5]. In this study, the lanthanides-doped luminescent nanocrystals of Er^{3+}/Yb^{3+} doped SrF_2 were initially crystallized in the SBBO GC micro-particles, and then through a facile in-situ etching method, the novel NIR GC photocatalysts with a superficial coating of BiOCl nanosheets in-situ grown on the surface of the SBBO GC were synthesized. These NIR GC photocatalysts can efficiently harvest the NIR photons and emit strong upconversion luminescence for photocatalysis. The photodegradation rates of organic pollutants with the NIR GC photocatalysts under NIR light are higher than those reported in most of the previous literatures. Furthermore, the NIR GC photocatalysts can be easily regenerated by using HCl etching again, which is suitable for large-scale synthesis.

2. Experimental section

2.1. Chemicals and material

The materials of BiOCl (99.5%), Bi_2O_3 (99%), $SrCO_3$ (99%), B_2O_3 (99%), NaF (99%), YF_3 (99.9%), Yb_2O_3 (99.9%), and Er_2O_3 (99.9%) were all purchased from Sinopharm chemical Reagent Co. Ltd (China) with analytical grade and they were used as received.

2.2. Preparation of upconversion GC

Lanthanides-doped SBBO GC was obtained from the following compositions in molar percentage (%): 22$SrCO_3$-22Bi_2O_3-22B_2O_3-15.5YF_3-16NaF-2Yb_2O_3-0.5Er_2O_3, and fabricated with one step (Fig. 1), and the mass of each component are: 8.57 g $SrCO_3$, 27.06 g Bi_2O_3, 4.04 g B_2O_3, 5.97 g YF_3, 1.77 g NaF, 2.08 g Yb_2O_3, 0.50 g Er_2O_3. The added Y^{3+} could dope into SrF_2 lattice to form SrY_xF_y with stronger luminescent properties, which improved the whole luminescence of GC [16]. Moreover, Y^{3+} could also dope into BiOCl to reduce its band gap [17]. Considering that fluorine was easy to volatilize, excessive fluorine was added in the form of NaF. The SBBO GC was prepared by a melt-quenching method. The well ground stoichiometric chemicals were completely mixed and crashed in ball crusher (MM400, Germany) for 5 min. The obtained raw mixture (total mass: 50 g) was put into a

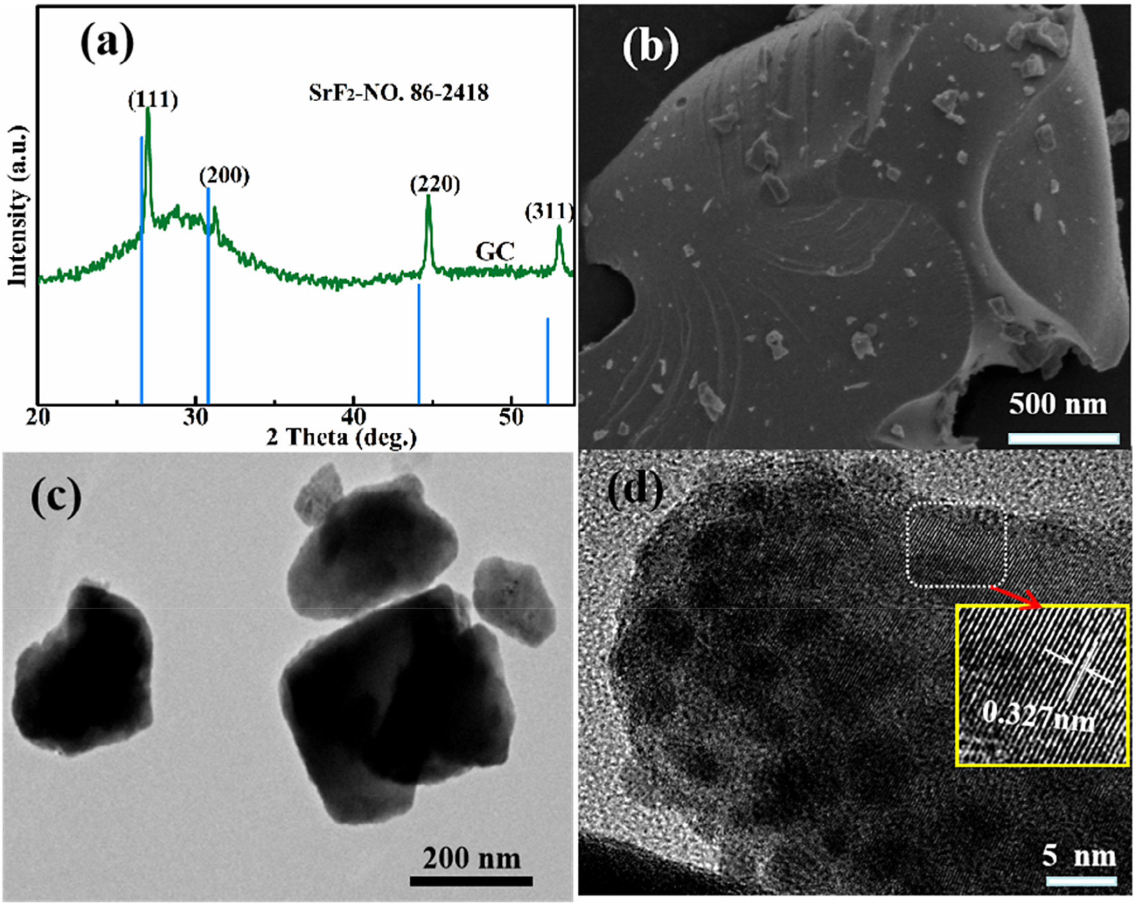

Fig. 2. Typical XRD patterns of the GC powder, (b) SEM image of the GC powder, (c) TEM, and (d) HRTEM images of GC powder.

crucible and melted at 1200 °C in air for 30 min. The melt was then poured on a 300 °C pre-heated copper mold, and the bulk molding upconversion GC was formed after annealing at 300 °C for 120 min. Afterwards, the bulk molding self-crystallized upconversion GC was milled in ball crusher (M100, Germany) for 30 min to obtain micron-scale upconversion SBBO GC powders.

2.3. Preparation of NIR GC photocatalyst

The SBBO GC powders were placed in the excessive HCl aqueous solution with concentration of 0.05 mol/L and stirred at a speed of 500 r/min for 0, 1, 5, 10, 15, 30, and 60 min. After that, the NIR GC photocatalysts samples were obtained with washing and drying, which were labeled as GC, GC1, GC5, GC10, GC15, GC30, and GC60.

2.4. Characterizations

The crystal structures of the samples were identified by X-ray diffraction (XRD) on a Bruker D8 Advance X-ray diffractometer at 40 kV and 40 mA using Cu Kα radiation (λ = 1.5406 Å). The morphologies and microstructures were characterized with the Sirion 200 field emission scanning electron microscope (FESEM) equipped with the energy-dispersive spectroscopy (EDS) instrument, and a TALOS F200X transmission electron microscope (TEM) instrument. The particle size was test by using Delsa Nano particle and zeta potential analyzer (Beckman Coulter, CA, USA). Analysis of element content and composition of photocatalysts were detected by X-ray fluorescence (Epsilon X3, Netherlands). The surface analysis was studied by X-ray photoelectron spectroscopy (XPS, Kratos Axis Ultra DLD), and all the binding energies were calibrated with the C 1 s peak at 284.8 eV. The absorption spectra were performed on the Lambda 950 UV-vis-NIR spectrophotometer, and the band gap energy was calculated referring to Tauc's formula. Room temperature upconversion fluorescence spectra were measured by a Hitachi F-7000 fluorescence spectrophotometer equipped with a 980 nm semiconductor solid laser with tunable power. Photoluminescence spectra (PL) were recorded at room temperature on a Hitachi F-7000 fluorescence spectrophotometer with excitation wavelength of 300 nm. The Brunauer-Emmett-Teller (BET) specific surface areas of the GC, GC1 and GC15 were analysis by a Quantachrome Autosorb-IQ gas adsorption apparatus at 77 K. The Raman microscope mapping result of GC15 was detected by Raman imaging combined with emission scanning electron microscope (TESCAN-MAIA3/ WITEC/ MAIA3 GMU model 2016). The upconversion decay curves were tested by a fluorescence spectrophotometer (FluoroMax Plus) equipped with a pulsed 980 nm laser excitation (MDL-III-980-2 W). The photodegradation intermediates of norfloxacin and MO were quantified by a nano-liquid chromatography (UltiMate3000 RSLCnano Liquid Chromatography/maXis impact UHR-TOF MS, USA).

2.5. Photocatalytic activities

The photocatalytic activities of the samples were evaluated by the decomposition of methyl orange (MO) (10 mg/L, 20 mL) and norfloxacin (20 mg/L, 20 mL) under NIR light (λ ≥ 780 nm) irradiations (provided by a 1000 W high pressure mercury lamp) and UV-vis-NIR light irradiations (provided by 500 W xenon lamp), as shown in Fig. S1. 20 mg of the samples were added in the MO and norfloxacin aqueous solutions. Before irradiation, the mixtures were kept in the dark with magnetic stirring for 2 h to establish an adsorption/desorption equilibrium. Every interval of time, 2 mL of the mixtures were collected and centrifuged. The changed absorption peak intensities of MO and norfloxacin supernatants at 464 nm and 270 nm were detected by a UV-vis spectrophotometer (Hitachi U-3900). In the photoactivity test for ·OH radical generation, terephthalic acid (TA, 4×10^{-4} mol/L in a 2×10^{-3} mol/L NaOH solution) was used, and the photoactivity test for $O_2\cdot^-$ radical generation was used nitro bluetetrazolium chloride (NBT, 1×10^{-3} mol/L), both of the test methods were similar to those mentioned above for the MO and norfloxacin degradations.

3. Results and discussion

3.1. Characterization of the GC

Fig. 2a shows the XRD spectrum of the GC, and all the diffraction peaks are attributed to the single-phase of SrF_2 (JCPDS Card No. 86-2418), demonstrating that the SrF_2 crystals have been generated in GC via glass self-crystallization [18]. In comparison to the standard PDF card No. 86-2418 of SrF_2, the diffraction peaks of the SrF_2 in GC have been redshifted to higher angles (Table S1), meaning the lattice parameters are decreased and some Sr^{2+} ions have been replaced by other ions with smaller radii, leading to the shrinking of the host lattice [16]. The SEM image of the GC particles is shown in Fig. 2b, and it can be found that its surface is smooth. Fig. 2c shows the TEM image of the GC particles, and some irregular nanoparticles with an average size of 200 nm are present. The enlarged morphology is shown in Fig. 2d, many black dots with size less than 5 nm embedded deeply into the GC particles, which may be ascribed to the Bi_2O_3 quantum dots [11]. The UV-vis-NIR diffuse reflectance spectrum and the band gap (3.1 eV) of GC can be seen and calculated in Fig. S2, which provide the possibility of energy conversion and transmission during the further photocatalytic reaction. Surrounding the black dots in Fig. 2d, the provided high-resolution TEM (HRTEM) image contains the lattice space of 0.327 nm, and it is assigned to the (111) planes of SrF_2. Elemental analysis in Fig. S3 showed that the main elements of F^-, Sr^{2+}, Y^{3+}, Yb^{3+}, and Er^{3+} were enriched in the GC sample. The doping effect in SrF_2 may be originated from the substitution of Sr^{2+} (1.12 Å) ions by the Y^{3+} (0.89 Å), Yb^{3+} (0.86 Å), or Er^{3+} (0.88 Å) ions with smaller radii [19], which creates a favorable environment for the generation of upconversion luminescence.

3.2. Characterization of the NIR GC photocatalyst

The XRD patterns of the GC samples etched by 0.05 mol/L HCl at different times are shown in Fig. 3a. The crystallization peaks of BiOCl increase gradually as the prolongation of the leaching times from 1 to 60 min, and the crystallization peaks of SrF_2 in GC gradually weaken and disapper. After 30 min, BiOCl tends to be stable while SrF_2 still decreases. In order to clearly observe the structural changes during the growing process, TEM images are provided in Fig. S4. The photocatalyst particles become finer, and the amount and size of BiOCl nanosheets grown on the surface of GC are increased gradually as the prolongation of the leaching times from 1 to 60 min. Meanwhile, the content of GC matrix decreases, and more SrF_2 crystals in GC expose to the HCl solution, which leads to the gradual dissolution of SrF_2 (reaction (1)).

$$SrF_2 + 2\,HCl = SrCl_2 + 2\,HF \tag{1}$$

In general, Raman spectroscopy is a powerful experimental technique for probing the vibrational and structural properties of crystals. Fig. S5a shows the Raman spectra of the GC and GC15 samples, and the strong Raman band at 144.9 cm^{-1} is assigned to the A_{1g} internal Bi-Cl stretching mode [20]. The most notable Raman band at 248 cm^{-1} for both GC and GC15 compositions is assigned to the Bi-O bonds vibrations in BiO_3 and BiO_6 units in the glass network [21]. The Raman microscope mapping of GC15 is shown in Fig. S5b, c. It can be distinguished that the green part of the GC15 surface belongs to BiOCl, and the red part in the middle attributed to the GC structure according to Raman characteristics [20,21]. The Raman data also show that, after BiOCl precipitation, the content of GC decreases by HCl etching, but this remaining GC structure has a low phonon energy of 248 cm^{-1}, which is conducive to producing high efficiency of upconversion luminescence.

The upconversion luminescence spectra of the etched GC samples under the excitation wavelength of 980 nm are shown in Fig. 3b. Quite evidently, it can be seen the strong intensities of the upconversion emissions of the GC and the etched GC samples, which are originated from the significantly enhanced luminescence efficiency of the Y^{3+}, Yb^{3+}, or Er^{3+} doped massive SrF_2 nanocrystals separated out from the GC, which create an environment with low phonon energy to promote efficient upconversion luminescence [16,22]. As shown in the upconversion luminescence spectra, the red (656 nm), green (523 and 540 nm), violet (408 nm), and UV (379 nm) light emissions are attributed to the ${}^4F_{9/2} \rightarrow {}^4I_{15/2}$, ${}^4S_{3/2} \rightarrow {}^4I_{15/2}$, ${}^2H_{11/2} \rightarrow {}^4I_{15/2}$, ${}^2H_{9/2} \rightarrow {}^4I_{15/2}$, and ${}^4G_{11/2} \rightarrow {}^4I_{15/2}$ transitions of Er^{3+} ions, respectively [7]. Interestingly, it can be clearly seen that, after BiOCl precipitates formed on the surface of the etched GC, the upconversion luminescence intensity is largely enhanced compared with those of GC. But further extend the etching time, the upconversion luminescence gradually weakens, and its intensity is even lower than that of GC after more than 15 min etching. Fig. 3c and Fig. S6 show the optical image of the bright yellow-green upconversion emission light of the bulk GC and GC15 powder samples under 980 nm excitation. Owing to the excellent luminescent properties of GC, the innovative upconversion GC can be put potential applications in the field of solid laser, optical fiber, light-emitting diode illumination, and so on.

The decay curves of the green (540 nm, ${}^2H_{11/2} \rightarrow {}^4I_{15/2}$) and violet (408 nm, ${}^2H_{9/2} \rightarrow {}^4I_{15/2}$) light of the GC and the etched GC (GC15) samples under 980 nm excitation are shown in Fig. 3d and e, respectively. The fitting parameters of the decay curves for GC and GC15 are shown in Table S2. It can be clearly seen that the average fluorescence lifetime (τ_{avg}) is dramatically increased from 27.17 to 165.27 ms after etching, which indicates that the surface-quenching effect in GC15 have been suppressed, and the reasonable explanation is related to the decreased surface defects modulated by the BiOCl growth [23]. For the τ_{avg} of 408 nm violet light, the values increased slightly from 0.4 to 0.75 ms, which is attribute to the direct absorption by BiOCl.

Fig. 4a shows the SEM images of the GC15 photocatalyst, and many irregular particles with sizes of 0.5~8 μm were present. From the enlarged particle morphology (Fig. 4b–d), it can be observed that the surface of GC15 is wrapped by a large number of nanosheets, especially, these nanosheets were vertically aligned and densely cross-linked (Fig. 4b, c), which make full exposure of reactive sites to promote photocatalytic reaction. The TEM and HRTEM images of the GC15 were shown in Fig. 4d–g, and the lattice fringes of 0.275 nm and 0.742 nm are respectively consistent with the (110) and (001) planes of BiOCl, meaning all the nanosheets are attributed to BiOCl. Moreover, some dislocations and distortions seem to be present on the basal plane (Fig. S7a, b), which may reveal a defect-rich structure. These surface pit defects could afford more accessible coordination-unsaturated atoms with dangling bonds as active sites that can contribute to the separation of electron-hole (e^--h^+) pairs [24]. In addition, the results (Fig. S7c) showed that the whole PL peaks of GC15 are weaker than those of pure BiOCl and GC, which indicates that the separation efficiency of photogenerated electron–hole pairs of GC15 is the highest among the samples [25].

Fig. 5 shows the EDS mapping results of the GC15. From Fig. 5a–e, it can be clearly seen that the centers are rich in the elements of O and Bi, while the Cl element only locates in superficial layer, mainly because the concentrations of O and Bi in the GC are higher than those in the superficial layer of BiOCl. Furthermore, as shown in Fig. 5f–j, it is noted that the signals of Sr, Y, and F elements reveal significant enrichment. Combining with the XRD analysis (Fig. 3a), we believe that the Y^{3+} ions have been doped into the SrF_2 crystal phase, and the size of the

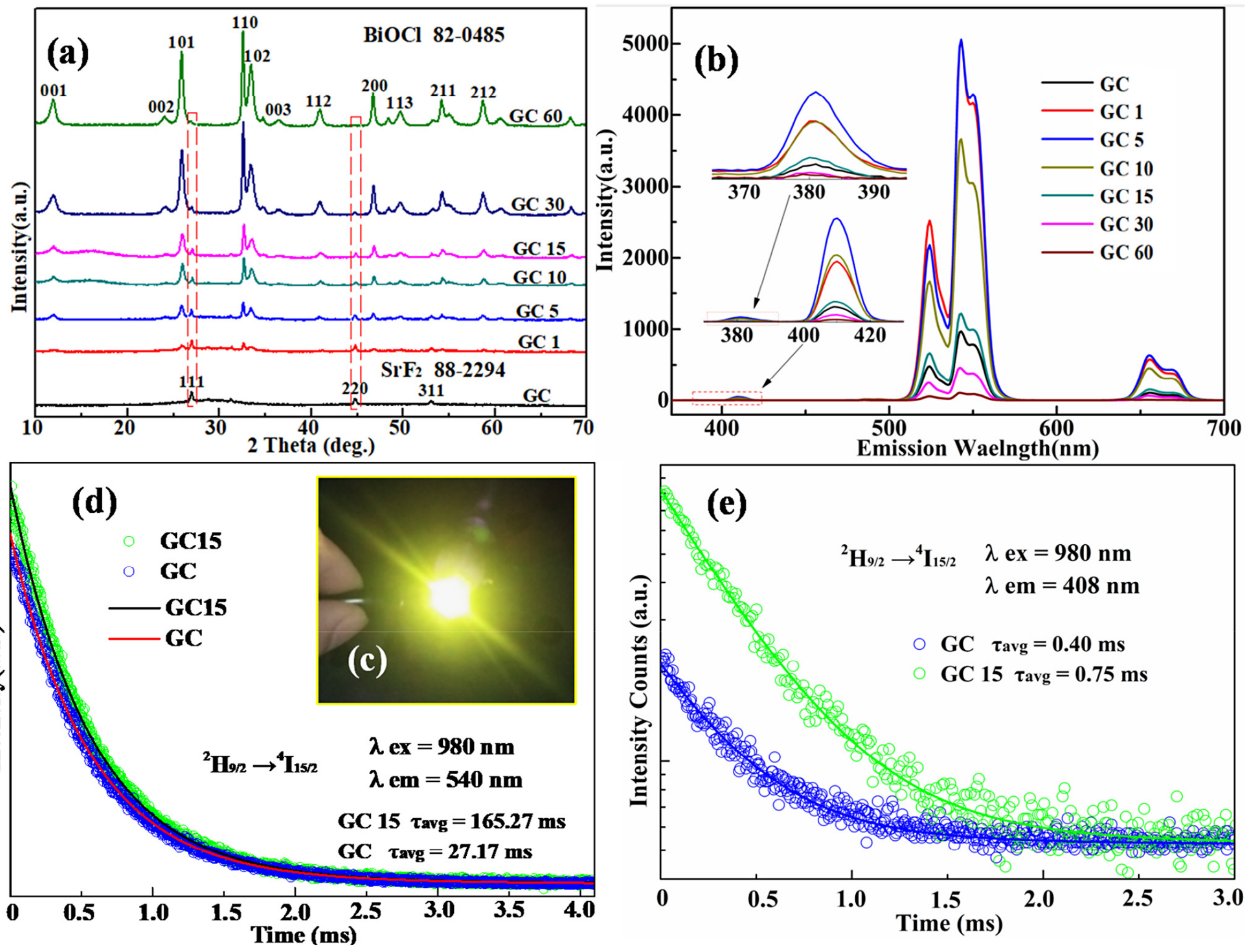

Fig. 3. (a) The XRD spectra, (b) upconversion luminescence spectra of GC, GC1, GC5, GC10, GC15, GC30, and GC60; (c) Optical image of the upconversion emission of under 980 nm excitation of GC; The fluorescence decay curves of (d) Er^{3+} (λex = 980 nm), Er^{3+}(λem = 540 nm), and (e) Er^{3+} (λex = 980 nm), Er^{3+} (λem = 408 nm) emitting states of GC and GC15.

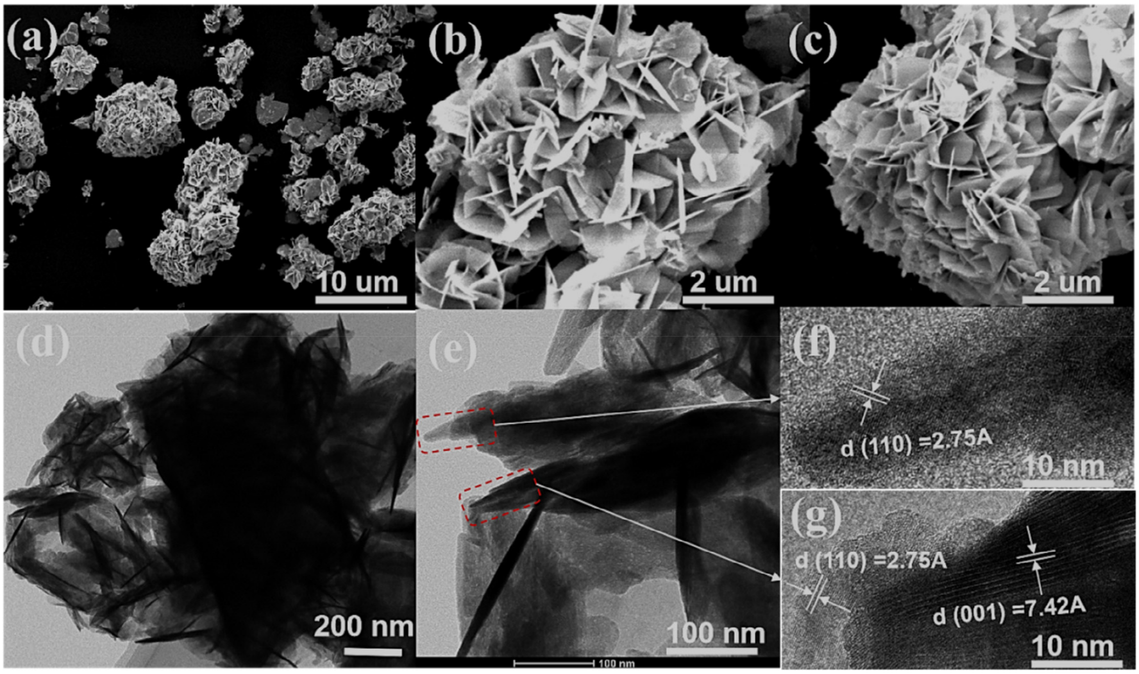

Fig. 4. (a)–(c) SEM and (d)–(h) TEM of GC attacked by 0.05 mol/L HCl at 15 min (GC15).

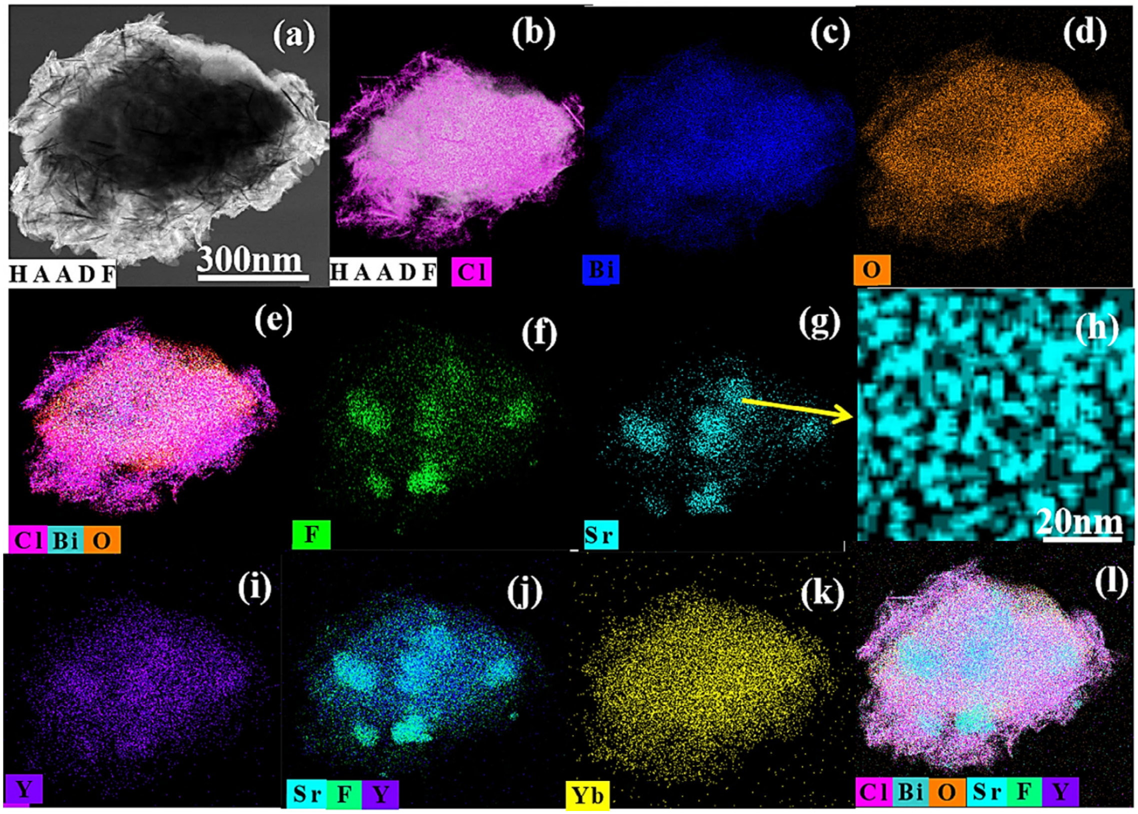

Fig. 5. (a) The HAADF-STEM image and the elemental distribution mapping results for (b) Cl, (c) Bi, (d) O, (e) Cl + Bi + O, (f) F, (g) Sr, (h) magnification of Sr, (i) Y, (j) Sr + F + Y, (k) Yb, and (l) Cl + Bi + O + Sr + F + Y of the GC15.

obtained SrY_xF_y crystals is about 100 nm, which further consist of a large number of nanocrystals of about 5 nm located in the GC network (Fig. 5h). Fig. 5k shows that Yb is also distributed throughout the area of the surface BiOCl layer, indicating that Yb may have also been doped into BiOCl, as well as F, Er, Y (Fig. S8), and B (Fig. S9), which are in favor of improving the light utilization efficiency. Fig. 5l shows the overlay of Bi, O, Cl, Sr, F, and Y. It can be clearly seen that the GC is wrapped by a thin layer of BiOCl, and the luminescent nanocrystals of SrY_xF_y are precipitated in the center parts of GC. The entire system is conducive to the construction of the core-shell structure. As a result, the NIR-visible light can penetrate the surface BiOCl layer into the core luminescent matrices, and then the upconversion emissions with high energy photons are generated. We speculate that the existence of Bi_2O_3 quantum dots in GC may contribute to the band gap (Fig. S2), and it may be helpful to construct some potential heterojunctions between surface BiOCl layer and the center part of Bi_2O_3 quantum dots contained GC, which provide ways for electron-hole (e^--h^+) pair separation, and are beneficial to the utilization of the external radiation light and the internal upconversion light for photocatalysis.

The specific surface areas of the GC, GC10, and GC15 samples were further studied by the nitrogen adsorption-desorption experiments. As shown in Fig. 6a, GC10 and GC15 display type II adsorption-desorption isotherms, which are typical characteristics of macroporous materials composed of slit holes produced by aggregated nanosheets [26], and this can be confirmed by the above results of the SEM/TEM images (Figs. 3 and 4). The BET specific surface areas of GC and the etched GC are quite different. The GC sample has a low BET surface area of 1 m^2/g. After HCl etching, the BET surface area of GC10 is largely increased to the value of 18 m^2/g. This increment should be contributed by the pores produced in the etching process and the formed BiOCl nanosheets layer. As for GC15, its specific surface area (19 m^2/g) and pore size only increase slightly compared with those of GC10. Fig. 6b shows the particle size distributions of GC10 and GC15 based on the zeta potential analysis, and the particle size of GC15 is decreased from 628.3 nm of GC10 to 452.1 nm. Moreover, the zeta potential of GC samples changed obviously at different etching times (Fig. 6c). These unique structures may result in a high photocatalytic activity.

The survey scan XPS spectrum of GC15 shows that it contains the main elements of Bi, O, and Cl (Fig. 6d), and no obvious signals of the component elements of GC such as Sr, B, F, and Na (can be obtained by X-ray fluorescence spectrometer) can be detected (Table S3). In addition, the differences between the XPS and XRF results were caused by the different detection depths. It further proves that the surface of the GC is encapsulated by BiOCl to form a core-shell structure, and the presence of less amount of glass structure on the surface will not inhibit the active site, which is conducive to improving the photocatalytic efficiency. The high-resolution Bi 4f spectrum exhibits two individual peaks at 159.6 and 165.0 eV (Fig. S10a), which are assigned to the binding energies of Bi 4f $_{7/2}$ and Bi 4f $_{5/2}$, respectively. The Cl 2p spectrum is resolved into two peaks located at 197.70 and 199.30 eV (Fig. S10b), corresponding to Cl $2p_{3/2}$ and Cl $2p_{1/2}$ of BiOCl, respectively [26]. The weaker peak at 684.0 eV can be attributed to the native binding energy of a trace of SrF_2 remained on the superficial coating, however, the peak at 681.0 eV is reckoned to be consistent with the F^- ions in the interstitial lattice of BiOCl (Fig. S10c). The O1s spectrum of GC15 displayed in Fig. S10d shows a broad asymmetrical peak, which can be de-convoluted into two peaks at 530.3 and 532.3 eV, and they are attributed to crystal lattice O atoms (Bi-O) and B–O bonds in BiOCl (Fig. S9d), respectively [27], indicating that B may have probably doped into the BiOCl matrices. It is noted that the BiOCl layer probably doped with a certain amount of F^- and B^{3+} ions are very likely to exhibit enhanced photocatalytic activities.

The light absorption properties of pure BiOCl and GC15 were measured by UV-vis-NIR diffuse reflectance spectroscopy and shown in Fig. 6e. In comparison with the pure BiOCl, GC15 has a larger absorption edge of about 420 nm, indicating that the constituent of GC has

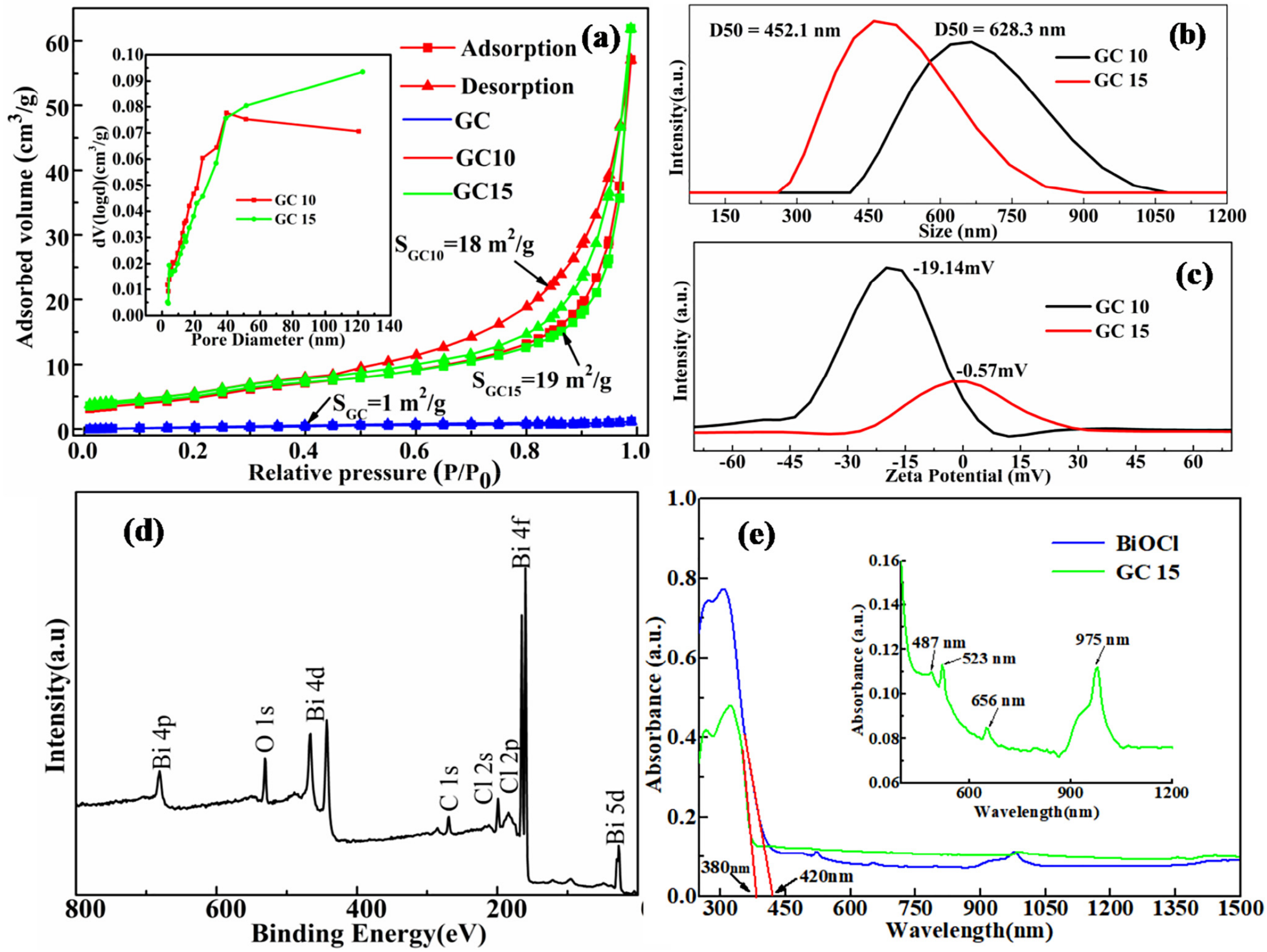

Fig. 6. (a) BET of GC, GC10, and GC15, (b) particle size (c) Zeta potential of GC10 and GC15, (d) XPS of GC15, and (e) UV-vis-NIR diffuse reflectance spectra of BiOCl and GC15.

a certain influence on the absorption edge of BiOCl because of the modification of F, B or lanthanides. Furthermore, there existed four relatively obvious absorption peaks at about 487, 523, 656, and 980 nm, which corresponded to the $^4F_{7/2} \rightarrow {}^4I_{15/2}$, $^2H_{11/2} \rightarrow {}^4I_{15/2}$, and $^4F_{9/2} \rightarrow {}^4I_{15/2}$ transitions of Er^{3+} ion and the $^2F_{5/2} \rightarrow {}^2F_{7/2}$ transitions of Yb^{3+} ion, respectively [28]. Compared with pure BiOCl, the absorption edge of GC15 increased from 380 to 420 nm, therefore, GC15 can absorb the upconversion emissions of violet (408 nm), UV (379 nm) and visible light (487, 523, and 656 nm) for the photocatalytic degradation of pollutants [23,29].

The mechanism of the facile in-situ etching process is inferred. The GC can be etched by HCl, and $BiCl_3$ is supposed to be formed, which is then hydrolyzed into BiOCl in 0.05 mol/L HCl solution (Reactions (2) and (3)), and rapidly recrystallized on the surface of GC, leading to the in-situ growing of BiOCl as the superficial coating. Meanwhile, the Yb^{3+}, Er^{3+}, F^-, and B^{3+} are probably doped into BiOCl during the process. As the content of GC matrix decreases resulting in the gradual dissolution of SrF_2 and its decrease of total amount in the GC. Furthermore, the dissolution of the superficial SrF_2 contributes to the exposure of the active sites of BiOCl.

$$Bi_2O_3 + 6\,HCl = 2\,BiCl_3 + 3\,H_2O \quad (2)$$

$$BiCl_3 + H_2O = BiOCl\downarrow + 2\,HCl \quad (3)$$

3.3. Photocatalytic activities

The NIR-driven photocatalytic performances of pure BiOCl, GC, GC1, GC5, GC10, GC15, GC30, and GC60 under NIR light irradiation ($\lambda \geq 780$ nm) were evaluated by the degradation of MO (Fig. 7a) and norfloxacin (Fig. 7b) in aqueous solutions. It can be observed that no obvious degradation occurred to the samples of pure BiOCl and GC, and only a much low degradation efficiency of 4.7% appeared over the GC1 sample. But for the GC photocatalysts with longer etching time, the C/C_0 conversion plots of MO decreased steadily under NIR irradiation, where the photodegradation rates increased gradually from 11% to 79% with the etching time increased from 5 to 15 min, which are significantly higher than those in recent reports [8,9,30,31], indicating that these etching GC systems possess superior photocatalytic activities under NIR irradiation. Further extending the etching time to 60 min, a decreased degradation rate of 53% was occurred to the GC60 sample, which should be caused by the greatly weakened upconversion luminescence (Fig. 3b) and the increased BiOCl particle size. Because the amount of GC matrix would decrease as the etching time increased, which resulted in the weak upconversion luminescence, and thus the available light energy from NIR light for photocatalysis was decreased. Similar degradation performances also occurred in norfloxacin degradation. As shown in Fig. 7b, a relatively high degradation efficiency of 66% was obtained for the GC15 sample while no degradation could be observed over the pure BiOCl. It should be noted that the obtained removal rates of 66% (antibiotic norfloxacin) and 79% (methyl orange)

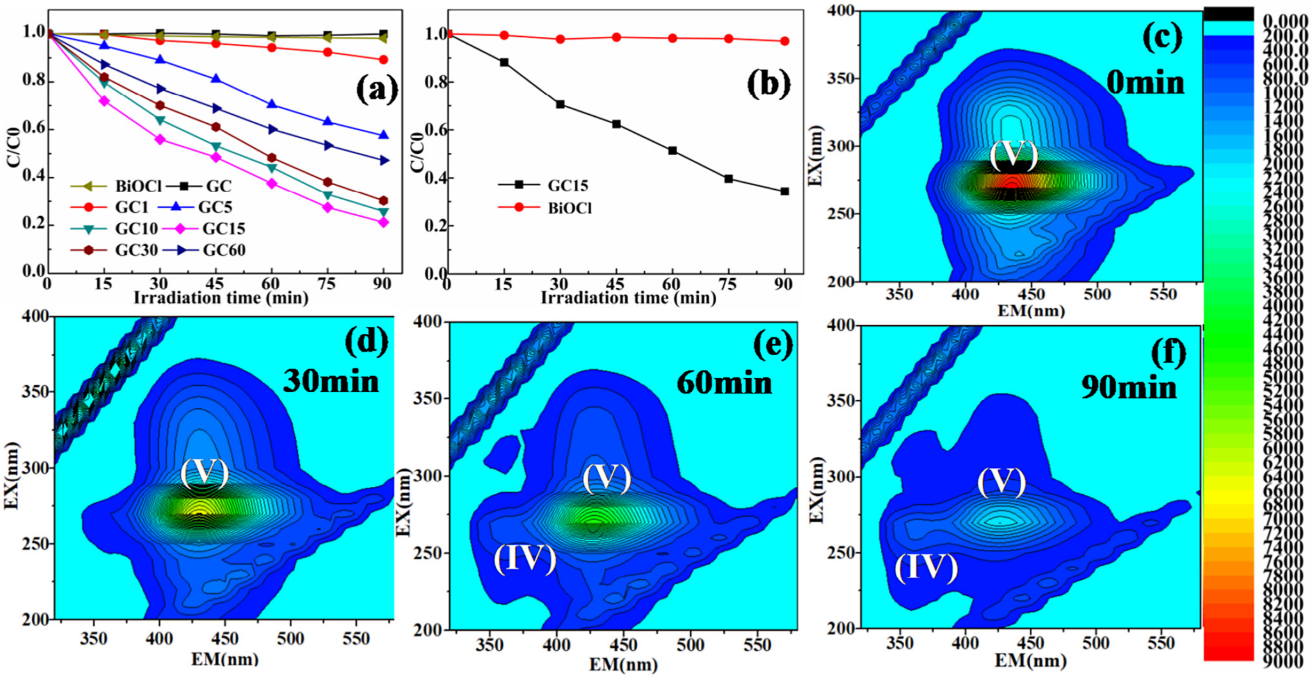

Fig. 7. C/C_0 conversion plots of MO (a) for pure BiOCl, GC, GC1, GC5, GC10, GC15, GC30, and GC60 under NIR (λ ≥ 780 nm) light irradiation. (b) C/C_0 conversion plots of norfloxacin for pure BiOCl and GC15 under NIR (λ ≥ 780 nm) light irradiation. EEM fluorescence spectra of norfloxacin for BiOCl and GC15 under NIR (λ ≥ 780 nm) light irradiation: (c) 0, (d) 30, (e) 60, and (f) 90 min.

are much higher than those reported in most of the previous literatures (Table S4).

In order to further explore the photodegradation mechanism, the EEM fluorescence spectra of the norfloxacin at different degradation times are shown in Fig. 7c–f. Prior to irradiation, there is a strong fluorescence peak of region V (Ex/Em of 270/434 nm), which is attributed to the humic acid-like compounds included in the norfloxacin wastewater (Fig. 7c) [32]. After the irradiation, the fluorescence intensity of the humic acid-like compounds is evidently decreased, and the fluorescence peak is shifted to Ex/Em of 270/426 nm (region IV), meaning that most of the macromolecular structures of the humic-like compounds have been destroyed [33]. It is noted that the new fluorescence peak of region IV at Ex/Em of 270/364 nm is attributed to the protein-like containing tryptophan compounds, which is formed from the decomposition of the humic-like compounds [32].

The UV-vis-NIR-driven photocatalytic performances of pure BiOCl, GC, GC1, GC5, GC10, GC15, GC30, and GC60 were also evaluated by the degradation of MO and norfloxacin in aqueous solutions (Fig. 8). It can be observed that no obvious degradation over the sample of GC. But for the etched GC photocatalyst, the C/C_0 conversion plots of MO decreased largely under UV-vis-NIR light irradiation, and the photodegradation rates increased from 15% of GC1 to 85% of GC15. For the GC60 sample, the degradation rate was decreased to 60%. Similar degradation results also occurred in the norfloxacin degradation, and a high degradation rate of 82% was obtained for GC15 within 30 min irradiation, which is much higher than that (22%) over the pure BiOCl.

The EEM fluorescence spectra of the norfloxacin wastewater under UV-vis-NIR irradiation are shown in Fig. 8c–d. The resultant EEM spectra was significantly different from those under NIR irradiation, where the fluorescence peak of the humic acid-like compounds at Ex/Em of 270/434 nm was even disappeared after 15 min irradiation. Meanwhile, a new fluorescence peak attributed to the protein-like containing tryptophan compounds at 270/364 nm was transformed from the decomposition of the humic acid-like compounds. As the irradiation time increased, this new fluorescence peak gradually decreased, and after 45 min, all the humic acid-like compounds and the protein-like containing tryptophan compounds were degraded and disappeared.

To elucidate the degradation route of norfloxacin, HPLC-MS was performed after 30 min of degradation over GC15 under UV-vis-NIR. Fig. S11a–c showed the MS spectra of the degraded norfloxacin, and the micromolecule substances were produced from norfloxacin (M/Z = 319). In addition, we try to estimate the possible degradation path to understand the photodegradation process of norfloxacin (Fig. S11d). The major pathways involved in degradation are defluorination, ring opening and decarboxylation. The product from photodegradation of MO has been also studied by LC-MS (Fig. S12a). After irradiation, a small amount of residual MO (m/z = 304) and some micromolecular compounds at m/z = 227, 114, 112, and 69 were detected. The proposed degradation pathway of MO is shown in Fig. S12b.

The $\cdot OH$ and $O_2\cdot^-$ trapping fluorescence spectra of the TA and BNT solution containing GC15 under UV-vis-NIR light irradiation are shown in Fig. 8e, f. It can be found that both of $\cdot OH$ and $O_2\cdot^-$ radicals increase markedly as the irradiation time extended. To further evaluate the effect of active species on the degradation of MO, the trapping experiments using quenchers were performed. Benzoquinone (BQ, 0.5 mM) and tert-butylalcohol (TBA, 6 mM) were selected as scavengers for $O_2\cdot^-$ and $\cdot OH$, respectively. The reaction conditions were the same as that of the synergetic photocatalysis reaction except to the addition of radical scavengers into the reaction suspension. As seen in Fig. S13, the results show that the MO removal rates over GC15, GC15 + BQ, and GC15 + TBA are 88%, 8%, and 79%. The photocatalytic decomposition rate over GC15 was suppressed to a greater extent when BQ is added as compared with that of TBA, indicating the higher influence of $O_2\cdot^-$ than that of $\cdot OH$ on MO degradation over GC15.

The photocatalytic enhancement mechanism for NIR GC photocatalyst was proposed (Fig. 9). The NIR GC photocatalysts can efficiently harvest the NIR photons and emit strong UV (379 nm), violet (408 nm), green (523 and 540 nm), and red (656 nm) emission light. According to the UV-vis-NIR diffuse reflectance spectra, the absorption edge of the NIR GC photocatalysts is about 420 nm, and there existed four relatively obvious absorption peaks at about 487, 523, 656, and 980 nm. Therefore, GC15 can utilize the upconversion emissions of violet (408 nm), UV (379 nm), visible light (487, 523, and 656 nm), and

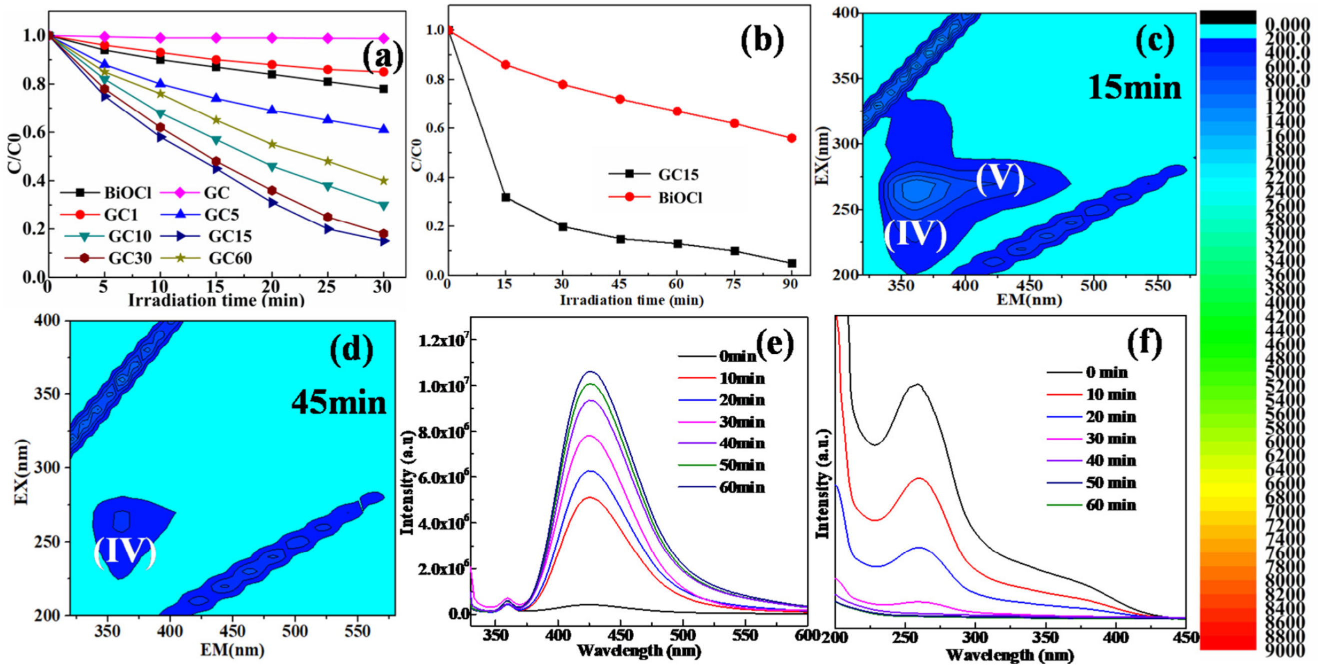

Fig. 8. C/C_0 conversion plots of MO (a) for pure BiOCl, GC, GC1, GC5, GC10, GC15, GC30, and GC60 under UV-vis-NIR light irradiation. (b) C/C_0 conversion plots of norfloxacin for pure BiOCl and GC15 under UV-vis-NIR light irradiation. EEM fluorescence spectra of norfloxacin for BiOCl and GC15 under UV-vis-NIR light irradiation: (c) 30 min, and (d) 45 min. (e) ·OH trapping fluorescence spectra of the terephthalic acid solution, and (f) $O_2\cdot^-$ trapping fluorescence spectra of the NBT containing GC15 under UV-vis-NIR light irradiation provided by a 1000 W high pressure mercury lamp.

the external environment light source with the wavelengths of 487 nm, 523 nm, 656 nm, and those less than 420 nm. Electrons can be excited and transferred from valence band (VB) to the conduction band (CB) of GC15 under those light irradiations. The ·OH radical can be generated through the reaction between holes and the surface adsorbed H_2O, and the electrons can be scavenged by the surface adsorbed O_2 to yield $O_2\cdot^-$ radicals. Then, the organic pollutants were attacked and destroyed by the ·OH and $O_2\cdot^-$ radicals during the photocatalytic process. The possible degradation pathways of norfloxacin and MO are shown in Figs. S11 and S12.

3.4. Photocatalyst regeneration

Fig. 10a shows the NIR (λ ≥ 780 nm) photocatalytic degradation cycling results, and the degradation efficiency over GC10 was changed from 74% to 68% after 5 cycles, indicating the high stability of the GC10 sample. But it should be noted that there is still a slight decrease after cycling 5 times. To further investigate the possibility of regeneration of the GC10 sample, the HCl etching experiment was performed again. The corresponding photocatalytic degradation results are shown in Fig. 10b. Interestingly, the photocatalytic activity was enhanced again, with the degradation efficiency increased from 68% to 79%. Although there is a slight decrease for the degradation efficiency after another further 5 cycling experiments, the resultant GC10 photocatalyst can be easily regenerated by HCl etching again. The morphology changes of the GC10 sample before and after regeneration are also observed by SEM. As shown in Fig. 10c, the surface of the first 5 recycled GC10 sample is still slightly encapsulated by abundant BiOCl nanosheets, but some of the collapse areas of the BiOCl sheets on the surface of GC may affect the active sites. After HCl etching, the surface structure is optimized to precipitate more and more dense BiOCl sheets (Fig. 10d), which improves the photocatalytic activity again.

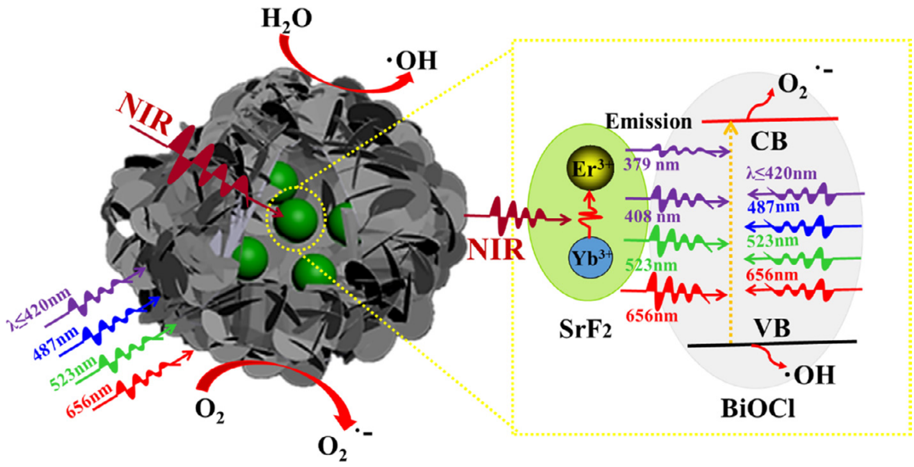

Fig. 9. The proposed photocatalytic enhancement schematic mechanism for NIR GC photocatalyst.

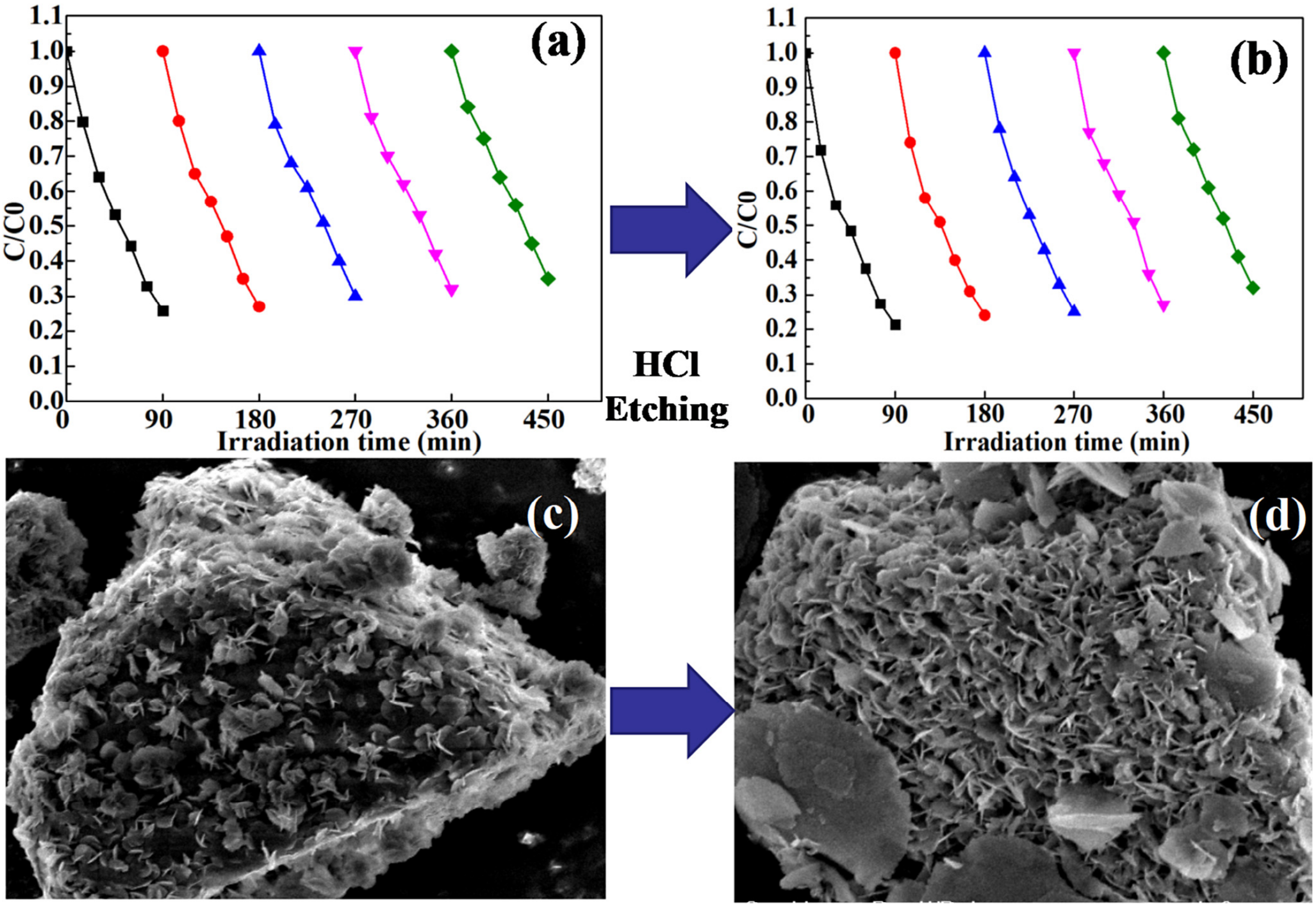

Fig. 10. Regeneration degradation curve of photocatalyst: 5 cyclic reactions of (a) GC10, (b) 5 times cycled GC10 by HCl etched for another 5 min, SEM of (c) 5 times cycled GC10 and, (d) 5 times cycled GC10 by HCl etched for another 5 min.

3.5. Prospects for large-scale fabrication of self-cleaning glass or NIR photocatalyst

The mass of the NIR GC photocatalyst in this study is about 45 g for a single experiment, and the amount of preparation scale can be multiplied. Less time required for NIR GC photocatalyst fabrication: melting glass (30 min), annealing (120 min), ball-milling (30 min), etching (15 min), drying (120 min). Meanwhile, and the main raw materials of $SrCO_3$, Bi_2O_3, B_2O_3, YF_3, and NaF are inexpensive and accessibly acquired, and the raw materials cost (according to the price of mass purchase) of fabricate NIR GC photocatalyst is 5.637 $/kg (Table S5).

Depending on the existing practical GC/glass melting technology, the NIR GC can be fabricated conveniently, and the NIR GC photocatalyst will be successfully obtained after the NIR GC treated in simple operations of milling and HCl etching (Fig. 1). Therefore, the NIR GC photocatalyst can be suitable for large-scale fabrication (self-cleaning glass pane or NIR photocatalyst powder) (Fig. S14).

4. Conclusions

In conclusion, an innovative self-crystallized upconversion luminescence SBBO GC was studied, and a facile in-situ etching method strategy was performed on the GC to synthesize the efficient NIR GC photocatalyst. In the GC, it is found that many SrF_2 crystals were generated in the glass self-crystallization process, where the Y^{3+}, Yb^{3+}, Er^{3+} ions were doped into SrF_2 to ensure the fabrication of strong upconversion luminescence. After etching, the BiOCl coating was in-situ formed on the remaining GC cores, leading to the great enhancement of the upconversion luminescence intensity, which may be caused by the decreased surface defects from the evidence of the longer fluorescence decay lifetime. Meanwhile, the XRD, XPS, and EDS mapping results proved that the Yb^{3+}, Er^{3+}, F^-, and B^{3+} ions could be doped into BiOCl during the facile in-situ etching method. There exist heterojunctions in the formed core-shell structure of the NIR GC photocatalyst, which provides possible ways for the electron-hole (e^--h^+) pair separation. Under NIR and UV-vis-NIR irradiations, the NIR photocatalyst efficiently harvests the light energy to exhibit high photocatalytic activities in the degradation of MO and norfloxacin. Furthermore, it is worth mentioning that the NIR GC photocatalyst can be easily regenerated and suitable for large-scale fabrication.

Declaration of Competing Interest

The authors declare that they have no known competing financial interests or personal relationships that could have appeared to influence the work reported in this paper.

Acknowledgement

This work was financially supported by the National Natural Science Foundation of China (No. 21876110 and 21607101).

Appendix A. Supplementary data

Supplementary data to this article can be found online at https://doi.org/10.1016/j.cej.2020.124877.

References

[1] Z. Wang, C. Li, K. Domen, Chem. Soc. Rev. 48 (2019) 2109–2125.
[2] J. Luo, S. Zhang, M. Sun, L. Yang, S. Luo, J.C. Crittenden, ACS Nano (2019).
[3] B.D. Ravetz, A.B. Pun, E.M. Churchill, D.N. Congreve, T. Rovis, L.M. Campos, Nature 565 (2019) 343–346.
[4] A.M. Smith, M.C. Mancini, S. Nie, Nat. Nanotechnol. 4 (2009) 710.
[5] Y. Liu, Y. Lu, X. Yang, X. Zheng, S. Wen, F. Wang, X. Vidal, J. Zhao, D. Liu, Z.J.N. Zhou, Nature 543 (2017) 229–233.
[6] Q. Tian, W. Yao, W. Wu, C. Jiang, Nanoscale Horiz. 4 (2019) 10–25.
[7] S. Huang, L. Gu, C. Miao, Z. Lou, N. Zhu, H. Yuan, A. Shan, J. Mater. Chem. A. 1 (2013).
[8] S. Ullah, E.P. Ferreira-Neto, C. Hazra, R. Parveen, H.D. Rojas-Mantilla, M.L. Calegaro, Y.E. Serge-Correales, U.P. Rodrigues-Filho, S.J.L. Ribeiro, Appl. Catal. B: Environ. 243 (2019) 121–135.
[9] G. Li, S. Huang, Y. Shen, Z. Lou, H. Yuan, N. Zhu, Y. Wei, Dalton Trans. 48 (2019) 9925–9929.
[10] K. Li, Y. Tang, Y. Xu, Y. Wang, Y. Huo, H. Li, J. Jia, Appl. Catal. B: Environ. 140–141 (2013) 179–188.
[11] S. Huang, L. Li, N. Zhu, Z. Lou, W. Liu, J. Cheng, H. Wang, P. Luo, H. Wang, J. Hazard. Mater. 382 (2019) 121041.
[12] S. Cao, C. Guo, Y. Lv, Y. Guo, Q. Liu, Nanotechnology 20 (2009) 275702.
[13] V.P. Singh, R. Vaish, J. Am. Chem. Soc. 101 (2018) 2901–2913.
[14] J. Barbier, L.M.D. Cranswick, J. Solid. State. Chem. 179 (2006).
[15] K. Majhi, K.B.R. Varma, K.J. Rao, J. Appl. Phys. 106 (2009).
[16] M.H. Imanieh, I.R. Martín, A. Nadarajah, J.G. Lawrence, V. Lavín, J. González-Platas, J. Lumin. 172 (2016) 201–207.
[17] X. Liu, H. Deng, W. Yao, Q. Jiang, J. Shen, J. Alloy. Compd. 651 (2015) 135–142.
[18] D. Chen, Y. Zhou, Z. Wan, H. Yu, H. Lu, Z. Ji, P. Huang, Phys. Chem. Chem. Phys. 17 (2015) 7100–7103.
[19] S. Geller, D.W.J.A.C. Mitchell, Acta Crystallogr. 12 (2010) 936-936.
[20] P. Xiao, J. Lou, H. Zhang, W. Song, X.L. Wu, H. Lin, J. Chen, S. Liu, X.J.C.S. Wang, Catal. Sci. Technol. 8 (2017) 1.
[21] R.V. Kumar, A. Edukondalu, B. Srinivas, G. Sriramulu, M.G. Krishna, K.S. Kumar, AIP Conf. Proc. 1665 (2015) 070038.
[22] G. Devarajulu, O. Ravi, C.M. Reddy, S.Z. Ali Ahamed, B.D.P. Raju, J. Lumin. 194 (2018) 499–506.
[23] S. Huang, Z. Lou, Z. Qi, N. Zhu, H. Yuan, Appl. Catal. B: Environ. 168–169 (2015) 313–321.
[24] J. Di, C. Chen, S.-Z. Yang, M. Ji, C. Yan, K. Gu, J. Xia, H. Li, S. Li, Z. Liu, J. Mater. Chem. A. 5 (2017) 14144–14151.
[25] L. Ding, R. Wei, H. Chen, J. Hu, J. Li, Appl. Catal. B: Environ. 172–173 (2015) 91–99.
[26] J. Li, M. Han, Y. Guo, F. Wang, C. Sun, Chem. Eng. J. 298 (2016) 300–308.
[27] D. Wu, S. Yue, W. Wang, T. An, G. Li, H.Y. Yip, H. Zhao, P.K. Wong, Appl. Catal. B: Environ. 192 (2016) 35–45.
[28] L. Zhen-Xing, S. Fu-Bo, Z. Tao, W. Hao-Shuai, S. Ling-Dong, Y.J.C.C. Chun-Hua, Chem. Commun. 47 (2011) 8109–8111.
[29] X. Guo, W. Di, C. Chen, C. Liu, X. Wang, W. Qin, Dalton Trans. 43 (2014) 1048–1054.
[30] L. Wang, C. Xia, T. Yang, H. Wang, N. Liu, C. Liang, Nanotechnology 31 (2020) 25601-25601.
[31] S. Liang, Y. Chang, Y. Wang, D. Zhang, X. Pu, Catal. Sci. Technol. 9 (2019) 2103–2110.
[32] W. Chen, P. Westerhoff, J. Leenheer, K. Booksh, Environ. Sci. Technol. 37 (2003) 5701–5710.
[33] S. Huang, S. Guo, Q. Wang, N. Zhu, Z. Lou, L. Li, A. Shan, H. Yuan, ACS Appl. Mater. Interfaces. 7 (2015) 20170–20178.